ABSTRACT

Title of Thesis: TECHNIQUES AND APPLICATIONS OF MESOSCOPIC FLUORESCENCE IMAGING

Yi Liu, Master of Science

Thesis Directed By: Yu Chen, Associate Professor, Fischell Department of Bioengineering

There is increasing interest towards visualization of tissue level with deep penetration depth in bioscience and medical research, mesoscopic imaging exchanges resolution for penetration depth, which offers hundreds of micrometer resolution and up to several millimeter penetration depth. By introducing fluorescence dyes or with intrinsic fluorescence, much higher contrast of images can be recorded compared to reflection imaging. To assess the characteristics of fluorescence imaging system, in the first part of this thesis I will discuss 3D printing technique as a novel phantom fabrication method which enables the fabrication of optically realistic and morphologically complex tissue-simulating phantoms for the development and evaluation of optical imaging products. In the second part, I will discuss about the techniques and applications of Angled fluorescence laminar optical tomography (aFLOT), a modified fluorescence tomographic imaging technique based on 3D reconstructions. To extend the capability of aFLOT to acquire more bioinformation besides, its availability for quantification and statistics has been studied. Some technical improvements of aFLOT system performance has also been taken by incorporating algorithms for imaging processing. In addition, examples of biomedical applications have been discussed to demonstrate the capability of aFLOT system in both bioscience and medical research field.

TECHNIQUES AND APPLICATIONS OF MESOSCOPIC FLUORESCENCE IMAGING

by

Yi Liu

Thesis submitted to the Faculty of the Graduate School of the
University of Maryland, College Park, in partial fulfillment
of the requirements for the degree of
Master of Science
2019

Advisory Committee:
Professor Yu Chen, Chair
Professor Joe Huang
Professor Giuliano Scarcelli

Acknowledgements

I would like to appreciate my parents' support for me for my graduate study at University of Maryland, College Park. And I also want to appreciate my wife Jing Huang's accompany during our life at the United States. My family has given me a strong power to do what I love and choose the right way of my life; I really appreciate them and wish one day I can go back home and get together with them.

I would like to appreciate Prof. Yu Chen for being my advisor during my four years' study at his lab. With his support on all the projects, from ideas to hands-on, I learned not only how to finish my job, but also how to think of questions. This helps me build great characteristics of critical thinking and solving, which may benefit my whole life.

In the 3D print project, I would like to appreciate Dr. Joshua Pfefer, Dr. Pejhman Ghassemi and Dr. Jianting Wang for their support for this project at FDA. It is a great experience for me to learn how to communicate and how to manage my work and time.

I would like to appreciate my committee members: Dr. Giuliano Scarcelli and Dr. Joe Huang. Your comments and supports during my graduate study at Fischell Department of Bionegineering helps me complete this thesis and my master study.

Finally, I would like to appreciate my lab-mates, Dr.Qinggong Tang, Dr.Bohan Wang, Dr. Udayakumar Kanniyappan, Brandon Gaitan, and Nitin Suresh. I hope everyone can have a bright future.

Table of Contents

Chapter 1: Introduction

Fluorescence imaging is a promising technique for clinical diagnosis with its capability of imaging in a high range of resolution and field of view. In this thesis, I will focus on mesoscopic imaging, which can acquire tens of micrometer level resolution with millimeter penetration depth. In this range, we are able to acquire functional information in tissue level. Some brief introduction of imaging fundamentals will be illustrated in this section.

1.1 Fluorescence Imaging

Fluorescence imaging is a tool developed since the first fluorescent dye fabricated in 1871. Its usefulness to life science applications has been demonstrated as biomolecular labels, cellular stains, ionic indicators and more. The concept of fluorescence microscopy relies on the use of fluorophore-containing molecules that emit light in either visible wavelength or another wavelength can be detected. The benefit of fluorescence imaging is that the targeted structures are illuminated while the undesired areas of the sample have only little fluorescence, which leads to easy targeting and high contrast [1].

1.2 Image Quality Characteristics

There are some image characteristics methods to better describe the performance of imaging systems. Resolution describes the limitation of the size to be detected by imaging systems, penetration depth describes the depth of target where can be detected with defined resolution. Due to the diffusion limitation of light, resolution and penetration depth are a pair of trade-off parameters. If we want to acquire high resolution images, we must sacrifice penetration depth. In mesoscopic imaging field, researchers prefer relatively deeper penetration depth to acquire 3D images with non-invasive imaging techniques. Contrast is another parameter to describe image quality, it is defined by the intensity of signal over the intensity of noises. Intuitively, higher contrast may lead to images with needed information highlighted. Compared to reflection imaging, fluorescence imaging has much higher contrast which makes it ideal for some bioscience and medical research. In the next chapter, I will first introduce one of my work on imaging

performance analysis with phantom fabrication. Since it is important to understand and assess the performance of imaging systems before applying it to specific applications, standard phantoms mimic biological tissue are introduced.

Chapter 2: Fluorescence Imaging and Phantom Fabrication

This chapter is based on the publication "Biomimetic 3D-printed neurovascular phantoms for near-infrared fluorescence imaging" by Liu, Y., Ghassemi, P., Depkon, A., Iacono, M.I., Lin, J., Mendoza, G., Wang, J., Tang, Q., Chen, Y. and Pfefer, T.J., in Biomedical Optics Express, 9(6), pp.2810-2824 (2018) [2].

Performance testing is important for researching imaging modalities, which includes fundamental image quality characteristics like resolution and contrast, as well as task-target tests. Non-biomimetic phantoms can be applied for standardization, and biomimetic phantoms may fill an important role in testing the performance of imaging systems. When used together, standard and biomimetic phantoms may provide complementary information that facilitates innovation and reduces the burden of regulatory testing while maintaining scientific rigor [3, 4]. In this study, I researched near-infrared fluorescence (NIRF) imaging devices which used the passive contrast agent Indocyanine Green (ICG) for clinical cerebral angiography.

2.1. Phantom Fabrication Methods

In order to generate phantoms incorporating realistic brain morphology, a previously published MRI-defined volumetric model of the human head has been used [5]. This model incorporates 15 segmented tissue types, including the four regions used in this study: gray matter, white matter, veins and arteries. Magnetic resonance angiography sequences (MRA) were acquired to enhance the visualization and segmentation of the arteries and the veins in the head. The sequence encodes flow direction and was optimized to highlight blood flowing in cranial direction, which resulted mostly in arteries being visible.

The maximum spatial resolution of the original MRI was 0.5 mm x 0.5 x 0.5 mm; thus, the segmentation was only limited to the large vessels discernable on the images, shown in Figure 1. A region of the segmented cerebral image volume in the frontal lobe was selected (as yellow box shown in Figure 1) to help ensure that the fabrication approach was manageable. This region includes the prefrontal cortex and is

supplied by polar and orbital frontal arteries; however, the primary vascular network in this region is the anterior portion of the superior sagittal sinus, with anterior frontal and frontopolar veins.

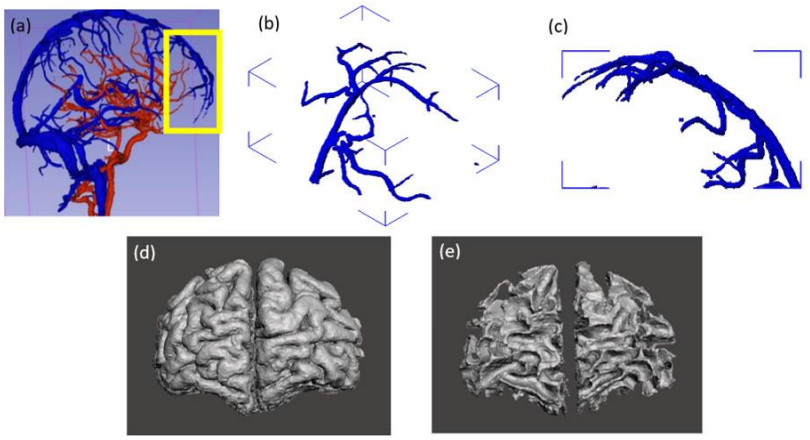

Fig. 1. Illustration of the main components of the digital neurovascular map generated from the MRI volumetric model [5]: (a) full network of larger arteries (red) and veins (blue), and frontal lobe region used in this study, including (b, c) vasculature, (d) grey matter, and (d) white matter.

Initially, we attempted using the raw MRI as the design of our cerebral phantom; however, the resolution of the commercial 3D printer is limited and can be as bad as 0.1 mm, especially when it prints complex geometry, it may leads to lots of unpredictable breaks. Therefore, with several trial, we made our irregular vasculature systems to be averaged around 1.5 mm diameter. We used the software Autodesk Meshmixer (Autodesk, San Rafael, CA) to modify the original MRI map. A Boolean method was applied for combination of vasculature system and gray matter/ white matter. To ensure all vessels are connected, since some vessels are not shown in the MRI, we manually connected these channels and ensure that all of them are open to the back of the phantom and able for injection. After all these pre-print design has been done, the model is smoothed and refined with Meshmixer [6].

Based on this vascular structure map, we created two phantoms, one is a homogenous rectangular matrix (109 mm x 84 mm x 39 mm) with a 3D network of channels from ~1.5 mm depth to the back of the phantom. This was performed in part as a preliminary test for the 3D vessel matrix. Additionally, this phantom could provide depth information with vasculature in different depths. The material for fabrication is same as white

matter. Another morphological-mimetic phantom is printed with two different materials (gray and white material) to mimic different optical properties of gray matter and white matter.

2.2 3D-printing Process

In this study, I first tried a commercial 3D printer FormLab Form 1+, it is capable of printing 10 cm x 10 cm x 10 cm phantoms with resolution as high as hundreds of micrometers. To test its capability to print channels, I designed several channel phantoms, since the horizontal resolution could be different to vertical resolution, the channels are printed in both horizontal and vertical direction. The results showed that only >0.8 mm diameter channels can be printed without block. The reason for this printer too hard to print the channel is the technique of printing, which is called stereolithography (SLA), by fusing liquid printing material into solid with high power ultraviolet laser. Therefore, there is some possibility of the material to be fused due to temperature or scattered light where it is not supposed to, especially the small channels.

Then, we used another commercial printer (Objet260 Connex3, Stratasys Inc., Eden Prairie, MN) for phantom fabrication. This printer is based on the "Polyjet" technique, in which UV light is used to cure droplets of liquid photopolymer from multiple heads that spray outlines of the printing part slice by slice. This technique has several advantages over other rapid prototyping techniques, including the ability to simultaneously print combinations of three different printing materials. Additionally, it can combine different concentration of white material and black material to build gray material with different degree, which leads to different scattering and absorption coefficients.

To measure optical properties of 3D printing materials, several 4 cm x 4 cm x 1mm slabs were printed. Diffuse reflectance and transmittance were measured from 700 to 100 nm using a dual beam integrating sphere spectrophotometer (Lambda 1050, PerkinElmer Inc., Hopkinton, MA). Absorption and reduced scattering coefficients were calculated at each wavelength using the inverse adding-doubling method [8]. Optical properties are shown in Figure 2 for a 100% white material, as well as a proprietary gray material

(RGD-8510) created from a mixture of the white and black materials. Both materials provided scattering coefficient levels in the 5-6 /cm range near 800 nm which is moderately good agreement with cerebral optical properties from the literature [8,9]. While the white material was used for the rectangular phantom, both white and gray materials were used to simulate corresponding brain matter regions of the curved-surface biomimetic phantom.

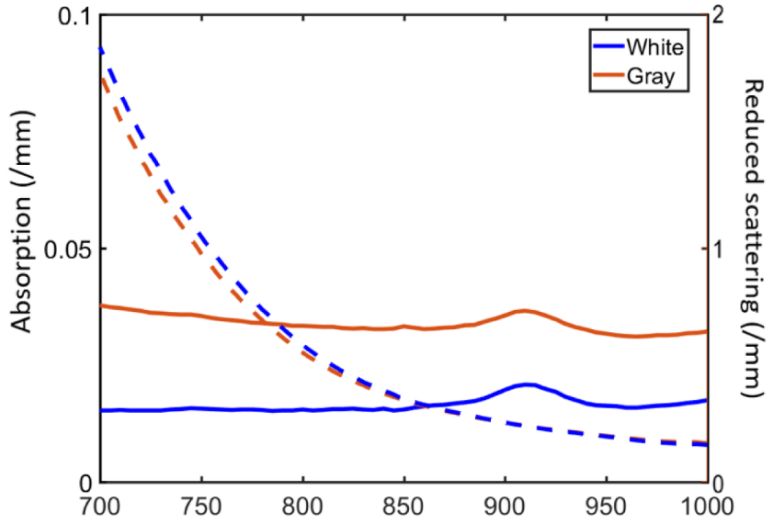

Fig. 2. Optical properties of combined 3D printing materials, including absorption and reduced scattering coefficients. Results are presented for a 100% white material as well as a mixture of white and black materials. (Absorption coefficient: solid line, units on the left; reduced scattering coefficient: dashed line, units on the right; blue lines: white material; red lines: mixture material).

After printing, the supporting materials were removed. The supporting material is generated in the program of the 3D printer to support the structural integrity of the printing sample during printing process. These materials are designed to be easily removed by light force of instruments or resolved by sodium solution. In this study, the phantom was cleaned first by soaking in a 2% sodium hydroxide and 1% sodium metasilicate solution (WaterWorks, Stratasys, Eden Prairie, MN) while the stirring was at a rate of 400 rpm for 2 days on the digital hotplate stirrer (SoCal BioMed, Newport Beach, CA). It is important to control the speed of stir as well as the time period since the printing material may also been resolved or softened by the sodium solution. Then, a 25G needle was applied to clean the channels carefully. For some channels, soft copper wires were applied to clean deep areas as well as twisted channels. After all channels were cleaned up, the phantom was then immersed in the sodium solution again for one day as final clean. Since

the channels are superficial and too hard to clean, in the final biomimetic phantom, the cleaning process induced two small holes in superficial vessels which were subsequently sealed with clear epoxy. The phantoms are sustainable for at least months and can be repeatedly injected/ cleaned of contrast agent, which makes this research consistent and convenient for further study.

2.3 Printed Phantoms

The printed phantoms are shown in Figure 3. The challenges for this printing process are the printing of twisted vasculature system due to the limitation of 3D printer's performance. To assess the printed phantoms integrity, microCT imaging is applied. From the stack of microCT images, we may visualize the leaks of the printed phantoms as well as the whole 3D structure of the phantom. Figure 3(d) showed the reconstructed 3D images of the cerebral phantom captured by microCT imaging.

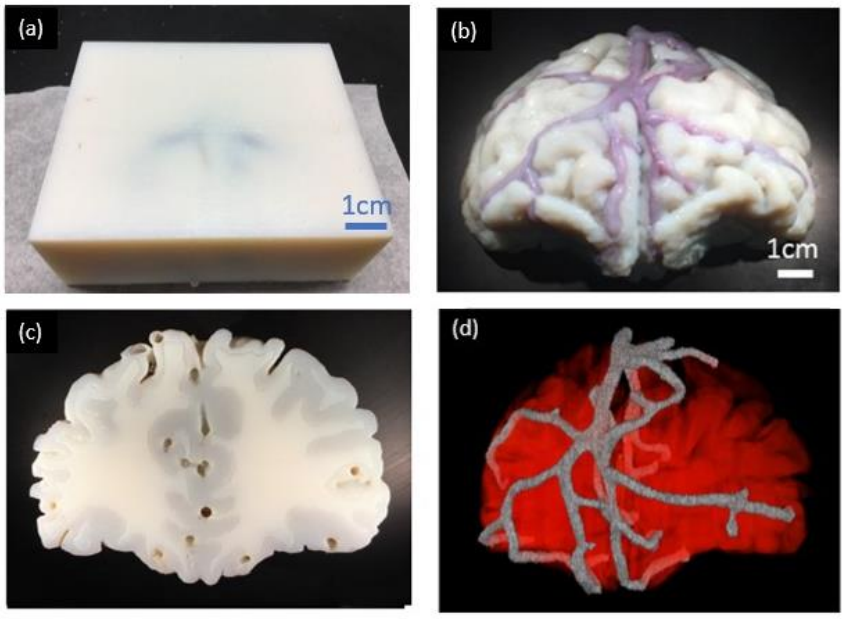

Fig. 3. (a) 3D-printed rectangular neurovascular phantom and (b) 3D-printed morphologically mimic neurovascular phantom, channels are filled with blood-ICG solution. (c) Back view of the morphologically mimic neurovascular phantom, (d) reconstructed micro-CT image of neurovascular phantom.

When the rectangular phantom was filled with blood solutions, superficial veins within 4 mm of the surface were visible under visible light illumination. Deeper internal arteries could not be readily visualized

due to high phantom turbidity. The biomimetic phantom exhibits blood-filled surface vasculature shown in Figure 3(b). While most vessels run along the surface of the gray matter at shallow area, several channels were deep into the white matter area. From the back view of the phantom, we may see the irregular border between white matter surrounding by gray matter, and also channels in both center which are arteries and edge areas which are veins. Since we did not separate veins and arteries in this study, for each injection for imaging, we may not read information of veins or arteries.

Using a custom Matlab routine for analysis of the printing performance, the morphology of the final biomimetic phantom was compared with the original MRI image volume and nominal phantom design which was modified from the original image and for our 3D print. Inner diameters of vessels at 22 representative locations are measured and compared, these locations including both arteries and veins, superficial and deep area, are shown in Figure 4. The mean enlargement in lumen diameter is ~66.8%. The comparison of the diameter of vessels in printed phantom. And the most channels were printed smaller than its design and the overall deviation is ~ 6%. There are two major reasons for this deviation: the resolution of the printer for channel printing and our post-printing cleaning method that there could still exist some supporting materials in the channels not thoroughly cleaned.

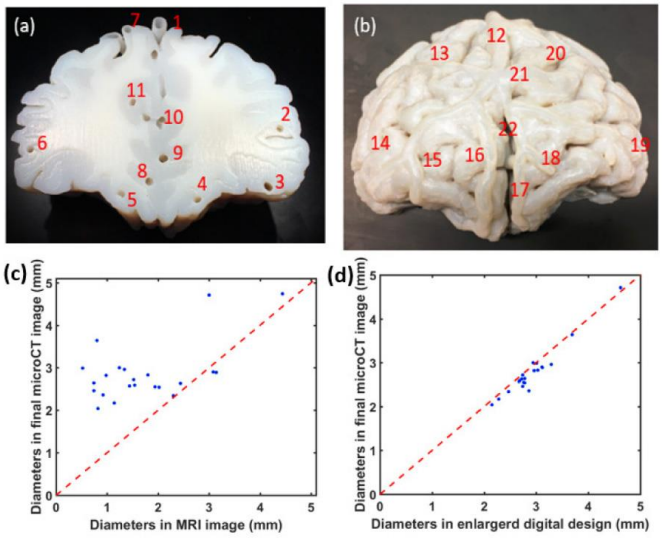

Fig. 4. (a)&(b) 22 typical locations of channels chosen for quantification of the channel sizes. (c) Comparison of vessel diameters between MRI image volume and final printed phantom; (d) vessel diameters in enlarged digital design and final printed phantom. Blue dots referred to different locations shown in (a)&(b).

2.4 Near-infrared Fluorescence Imaging

To analyze the performance of the biomimetic phantoms, and assess its capability for imaging system performance quantification, we performed NIRF imaging with a custom system built at Food and Drug Administration. The NIRF system is shown in Figure 5. which used a 1W light emitting diode (LED) source with central wavelength at 785 nm and 10 nm bandwidth (RLTMDL-785-1W-5, driver: RLTMxL PSU-LED, Roithner Lasertechnik GmbH, Vienna, Austria) providing 35 mW/cm^2 rradiance at the phantom surface. An 800-nm short-pass excitation filter (84-729, Edmund Optics, Barrington, NJ, USA) was placed in front of the LED to eliminate crosstalk between the light source and detected signals. Fluorescence emitted from the phantom was imaged through an 825 nm long-pass emission filter (86-078, Edmund Optics, Barrington, NJ, USA). The filtered light was detected by a 16-bit monochrome CCD camera (1200 x 1600 pixels, Alta U2000, Apogee Imaging Systems, Roseville, CA, USA). Camera control and recording was performed using Micro-Manager software (version 1.4.20, Univ. of California San Francisco, CA, USA). Image analysis was performed using Matlab.

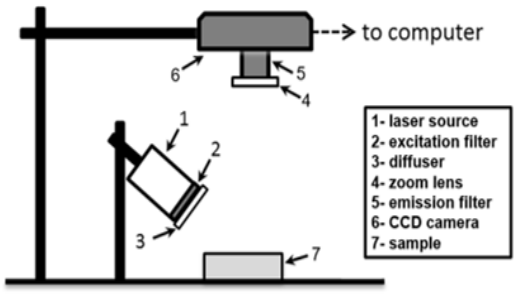

Fig. 5. Schematic illustrating layout of NIRF system.

Two different aqueous fluorescence solutions were prepared and injected into the channels of each phantom, separately: 1) ICG-bovine blood mixture with 3.2 μM of ICG (Pulsion Medical Inc., Powell, OH, USA), and 2) IR800-bovine blood mixture with 50 nM of IR800 (IRDye800 800CW Carboxylate, LI-COR, Lincoln, NE, USA) into the vascular channels of the brain phantom. In a previous in vivo animal study [10], the authors used 50 nM IR800 to quantify and assess IR800 performance. In clinics, the recommended dose for ICG angiography is 0.2 to 2 mg/kg with a maximum dose of 5 mg/kg/day [11]. Typically, ICG will be diluted to around 2.5 mg/ml for intravenous injection in humans [10]. In Liebert's study [12], researchers injected 11mg ICG diluted in 3 ml of saline intravenously into volunteers and measured the concentration of ICG in brain tissue to be about 1.7 μM. Other groups have used a minimum of 2.5 μM ICG for turbid phantom fabrication [13], and 0.08 μM to 1.03 μM in a blood vessel model [14]. Therefore, to better test the performance of our neurovascular phantoms, 50 nM IR800 and 3.2 μM ICG were chosen in our study. These solutions were then formulated with fresh defibrinated bovine blood (Quad Five, Ryegate, MT, USA). The filled phantom was then placed in a vacuum chamber for degassing for about 5 minutes, after which all the phantom openings on the bottom were sealed using hard glue.

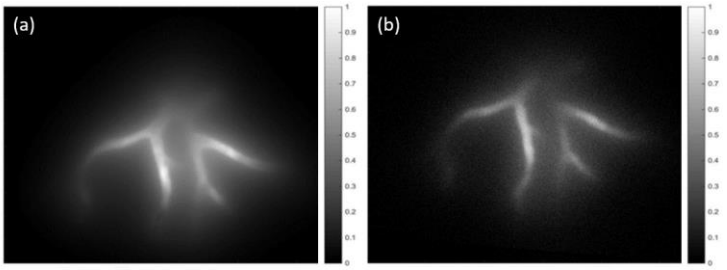

Fig. 6. NIRF images of rectangular neurovascular phantom (a) filled with (a) ICG and (b) IR800.

We imaged the both rectangular and morphologically biomimetic phantoms with the same system. Results are shown in Figure 6 and Figure 7. Well-defined and high-contrast vessels can be seen in the results in subsurface area. However, due to the diffusion of light, we may only visualize the signals to depths of up to 12 mm. The ICG image shows brighter signal compared to IR800. Image results also indicated that

both strong correlations in SNR with depth for both contrast agent, as 17.8 to 3.6 for ICG and 10.3 to 1.7 for IR800 from depth of 4 mm to 10 mm.

For the morphologically biomimetic phantom, results show well-defined, high-contrast vessels without the diffusion effect seen for subsurface vessels in the rectangular phantom. However, some variability in signal intensity along the channels is apparent. The white light images illustrate highly realistic brain surface morphology, including numerous cerebral sulci and superficial vasculature appearing as darker regions with low contrast. The combined white light and NIR fluorescence overlay images are seen in Figure 7. These images strongly highlight the vasculature against cerebral tissue structures, illustrating the utility of fluorescence imaging for intraoperative visualization and providing results with strong visual similarity to clinical images [15]. However, these images also show significant non-uniformity in NIRF signal intensity from the center of the image. Quantitative evaluation of SNR in corresponding high-contrast superficial vessel locations produced values of 158 for ICG versus 81 for IR800.

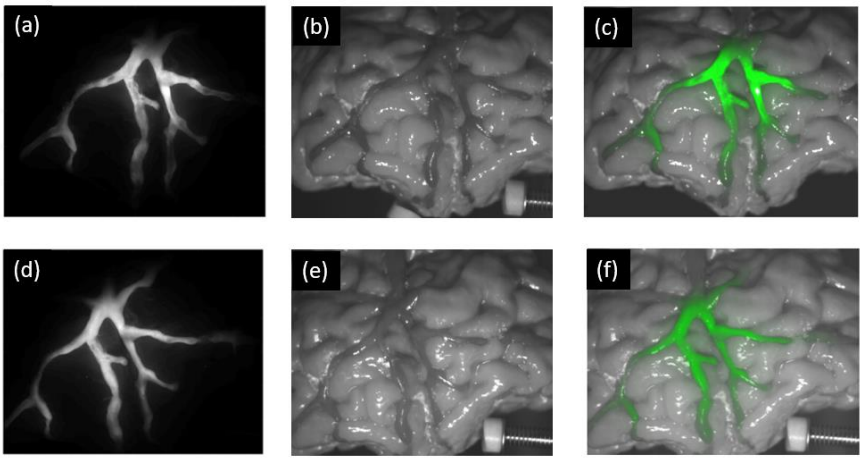

Fig. 7. NIRF (a,d), white light (b,e) and combined overlay images (c, f) of the biomimetic neurovascular phantom filled with ICG (a, b, c) and IR800 (d, e, f).

2.5 Discussion of Phantom Fabrication for Fluorescence Imaging Performance Test

Morphologically and optically realistic tissue-simulating phantoms represent powerful tools for development, evaluation, and translation of bioimaging techniques. The cerebral vascular phantoms in this study demonstrate the first successful fabrication of 3D vascularized models for biophotonic imaging

defined from a human subject image volume. The NIRF images appear strikingly realistic, particularly in comparison to prior cerebral phantoms for biophotonics [15, 16]. The rectangular phantom with vasculature system is particularly suited to quantification of imaging depth, and the morphologically mimetic phantom is more relevant to current clinical practices, which both demonstrated the promising application of 3D printing techniques for biomimetic phantom fabrication.

The steps of 3D printing required before and after the actual 3D printing process include a range of challenges: segmenting the image volume and process it to a 3D printable design; identifying the best design by error and trial of multiple printing, assess the results of printed phantoms and make modifications to the design for better prints; characterizing and selecting most suitable printing materials with biomimetic optical properties; and complicated post-printing cleaning process to minimize the damage to the phantoms. Although the challenges make the fabrication time-consuming, once the best design is achieved, it has high repeatability and consistency.

Besides the scientific parts, selecting a 3D printer typically involves evaluating trade-offs in functionality and performance. In this study, we used a relatively expensive commercial 3D printer Objet 260 (approximately $250,000) for phantom fabrication. The total material cost for fabrication of a single phantom is about $75. These prices are much higher compared to most desktop fused filament fabrication (FDM) and stereolithography (SLA) 3D printers. However, the benefits we can get is the availability of three materials printed simultaneously and high resolution. Besides, this printer can generate models that simulate heterogeneous, multi-component tissues, and generate both realistic surface and subsurface morphology, including channels or other structures. The disadvantage is that the material choices are limited since this 3D printer only supports the manufactured materials from the company which may limit to some applications if custom materials are needed. In the future, an ideal 3D printer for tissue phantom fabrication would provide both high resolution and the ability to simultaneously print multiple customized materials doped with absorbers and scatters.

In spite of the success in fabricating patient-specific neurovascular phantoms, several limitations remain. First, medical imaging systems capable of deep human tissue imaging, such as MRI, are not able to provide high accuracy or resolution of vasculatures. Secondly, 3D printers have limited resolution for printing hollow channels, particularly for irregular complex 3D geometry. Although nominal printing resolution values on the order of microns are often advertised, in our experience most printers are not able to reliably print patent linear channels smaller than 0.5 mm in diameter, or complex 3D networks with channels smaller than 1 mm diameter. Furthermore, even if printers were able to generate such channels, cleaning 3D printer support material from small-diameter and long, tortuous vessel segments can be difficult, and lead to damage in thin vessel walls. Therefore, some complimentary has to be taken for using 3D print technique for phantom fabrication, like enlarge the channel sizes.

Our phantom measurements provided preliminary insights into performance testing capabilities; however, a wide variety of other novel testing approaches may be implemented in the future. Unlike the simple phantom designs used to determine fundamental image quality metrics, realistic phantoms enable objective and subjective testing under realistic clinical conditions. Advanced testing based on true clinical diagnostic tasks involving pathology-simulating phantoms may enable more effective product evaluations. While additional improvements to increase the biological relevance of the phantoms are warranted, this work provides ample demonstration of the potential of 3D-printed biomimetic phantoms to enable performance assessment of bioimaging modalities under more realistic conditions than previously possible.

Chapter 3: Technologies of Fluorescence Laminar Optical Tomography

This chapter is based on publication "High-dynamic-range fluorescence laminar optical tomography (HDR-FLOT)." By Tang, Q., Liu, Y., Tsytsarev, V., Lin, J., Wang, B., Kanniyappan, U., Li, Z. and Chen, Y., on Biomedical optics express, 8(4), pp.2124-2137 (2017) [17].

3.1 Previous Research of Fluorescence Laminar Optical Tomography

Bridging the gap between micrometer and centimeter depth sensitivity and resolution, laminar optical tomography (LOT) combines diffuse optical tomography techniques for image reconstruction with a microscopy-based setup to allow imaging with ~100 μm resolution over depths of ~2 mm. [18]. LOT therefore surpasses the depth capabilities of optical coherence tomography and better suited to spectroscopy, as multiple wavelength can be used. LOT instrumentation acquires measurements that are equivalent to conventional DOT data, specifically, the scattered light emerging from tissue. Since diffusion approximation for DOT reconstruction is not applicable for LOT, Monte Carlo modeling is a better model for this short source-detection separation setup. For the FLOT setup in Prof. Chen's lab, around 300 image stacks will be recorded in 30 seconds for around 2 cm * 2cm * 2 mm 3D volume reconstruction.

Different from the LOT setup firstly introduced from Dr. Hillman's lab, Dr. Chao-Wei Chen has researched into angled FLOT (aFLOT) system and demonstrated better performance of 30-degree illumination (in tissue) compared to same directional source-detector pair [19, 20]. The setup of aFLOT system is shown in the Figure 8. My study in this chapter and next chapter are based on this setup.

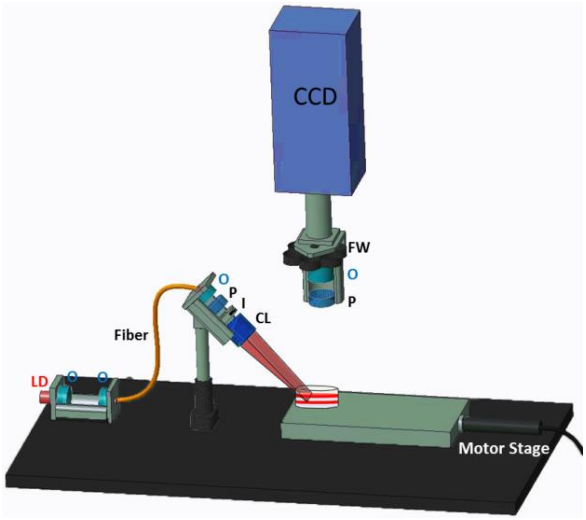

Fig. 8. Schematic of aFLOT imaging system. LD: laser diode; O: collimator; P: polarizer; I: iris; CL: cylindrical lens; FW: filter wheel;

3.2 High-dynamic Range FLOT

For the aFLOT system at our lab, it utilizes an electron-multiplying CCD (EMCCD) for imaging acquirement. Since deeper signals are always weaker than the surface area due to light diffusion. We must compromise between high intensity signals of deeper area with saturation at subsurface area or moderate signals at subsurface area but low penetration depth. The reason for this is the limited dynamic range of the camera and simultaneous signals from all depths for one-time reconstruction. One of the solutions for visualization of all depth is using high-dynamic range method which based on multiple-exposure scheme [21-23].

3.2.1 Methods of High-dynamic Range FLOT

A quick method for reconstruct a high-dynamic range image is to direct combine two images, one with long exposure time for deeper area visualization, one with short exposure time for surface area visualization. This method in some way works, if the goal is just for visualization. However, there are some problems for this method. First, the edge between two images, even some algorithms are applied to find the edge and combine two images well, there is still some unflatten value at the edge, if imaging targets lay on the edge,

it will make the image result terrible. Another problem is the quantification, that if some fluorescence intensity comparison needs to be taken, it was hard to do because two setups (two different exposure time) are taken for this one image. Therefore, some better imaging reconstruction methods should be taken for HDR image reconstruction.

The basic idea of HDR-FLOT is to implement 3D reconstruction in FLOT based on 2D HDR fluorescence images [24,25]. The first step to reconstruct 2D HDR images is to recover the CCD response function. The exposure X of a pixel can be defined as the product of irradiance E and the exposure time t, where irradiance E is influenced by the optical properties of the sample as well as illumination from the light source. From the CCD, we can obtain a digital number Z (CCD output), which is related with X at every pixel. We can define this relationship as CCD response function f. Since the background noise could cause deviation of the CCD response function, we first subtract the noise from the original CCD output, so that Z at every pixel will be:

$$\mathrm{Z} = Z_{sample} - Z_{background} \tag{1}$$

Z_{sample} are the values of samples from CCD, and $Z_{background}$ are background values in the corresponding images. Then, we can denote the response function as:

$$Z_{ij} = f(E_i t_j) \tag{2}$$

where i is the index of pixels and j is the index of exposure time. Since f is monotonic, we can rewrite Eq. (2) as:

$$f^{-1}(Z_{ij}) = E_i t_j \tag{3}$$

Taking the natural logarithm of both sides, we can obtain:

$$\ln f^{-1}(Z_{ij}) = lnE_i + lnt_j \tag{4}$$

Then, we can rewrite the equation with a defined function $g = \ln f^{-1}$ as:

$$g(Z_{ij}) = lnE_i + lnt_j \tag{5}$$

The parameters E and function g are unknown, but there is a linear relationship between $g(Z_{ij})$ and lnE_i. We change the problem to solving the quadratic objective function as follows:

$$O = \sum_{i=1}^{N}\sum_{j=1}^{T} w(Z)[g(Z_{ij}) - lnE_i - lnt_j]^2 + \sigma \quad (6)$$

where w(Z) is a weighting function. When the signal is low or saturated, the pixel value Z and exposure X may fit the response function poorly. Thus, we may give smaller weighting to those pixels. Simply, we can define w(Z) as [19]:

$$w(Z) = \begin{cases} Z - Z_{min} & for\ Z \le \frac{1}{2}(Z_{min} + Z_{max}) \\ Z_{max} - Z & for\ Z > \frac{1}{2}(Z_{min} + Z_{max}) \end{cases} \quad (7)$$

σ is introduced as a smoothness parameter to make sure that the function g is continuous and smooth [19]. The best estimate of CCD response function g will be obtained when O in Eq. (6) has its minimum value. The commonly used method to satisfy the equation is the least-square method for linear regression.

Because of the limited memory of a computer, we pick 2500 pixels instead of all the 512*512 pixels for calculation (i.e. the sampling rate is 1/10). The best estimate of the CCD response function g will be obtained when O reaches its minimum value. After the CCD response function g has been obtained, we can calculate irradiance E by Eq. (5). The weighting function w is introduced again here to give a higher weighting value to data at reliable ranges (the middle of the response function), but a lower value to the ranges near the extremes. Then, we can reconstruct the 2D HDR image as:

$$lnE^{HDR} = \frac{\sum_{i=1}^{N}\sum_{j=1}^{T} w(Z_{ij})[g(Z_{ij}) - lnt_j]}{\sum_{i=1}^{N}\sum_{j=1}^{T} w(Z_{ij})} \quad (8)$$

After that, we can obtain the 2D HDR image using all the images with different exposure times, and a series of 2D HDR images can be obtained at each scanning position which will be later used for 3D HDR-FLOT reconstruction.

3.2.2 Experimental Demonstration

To demonstrate the performance of HDR-FLOT for image reconstruction, and compared to non-HDR-FLOT system, we used an agar phantom with three 0.15 inner diameter glass capillaries inserted. These

three capillaries are filled with a large difference of fluorescence concentration, saying 2μM, 1μM and 0.2 μM Cy5.5 solution (Cyanine 5.5 azide, Lumiprobe Corporation). To mimic muscle tissue, 1.5g agar power with 0.3 mL 20& intralipid solution and 49 mL PBS buffer were mixed for phantom fabrication. After heated up in a microware for ~ 1minutes, the mixed liquid gel was poured into the petri dish for cool down. Then the filled capillaries are inserted into the agar phantom at the same depth side by side. Optical coherence tomography (OCT) will be utilized to ensure their depth are the same.

Figure 9. showed the OCT image results of the three capillaries as well as several 2D images with different exposure time. It is clear that with 100 ms exposure time, only the highest concentration capillary C1 has high contrast, and C3 signal is too low to visualize. On the other hand, when exposure time is as long as 2000 ms, C3 can be visualize but C1 and C2 saturated, and in this situation, we may not track back the real biological information of C1 and C2 which here is the fluorescence dye concentration. With HDR method, the CCD response curve is generated. It does not matter what phantoms or what exact concentration of contrast agents to be used for this reconstruction because this is the inner characteristics of the camera, which will not be affected by the objects it images at. With the help of response curve, we then reconstructed the HDR 2D image, shown in Figure 9(g). It is quite clear that we may visualize both high and low concentration of fluorescence dyes, and no saturations happen in this reconstructed image.

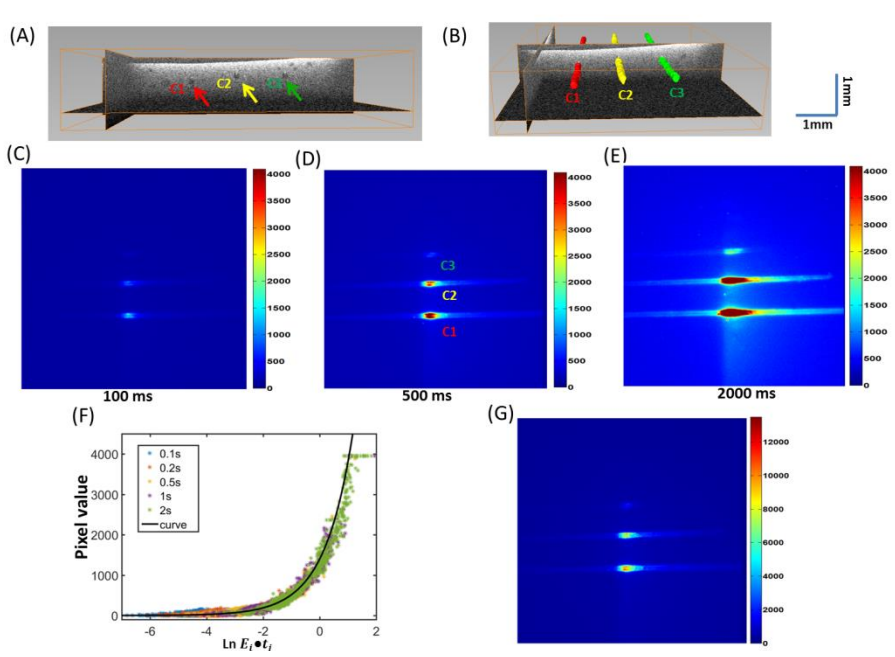

Fig. 9. (a) Image of the three capillaries filled with Cy 5.5 solution from OCT system indicated by the 3 arrows (red: 2 µM (C1), yellow: 1 µM (C2), green: 0.2 µM (C3)). (b) 3D rendered images of the 3 capillaries from OCT system. (c-e) 2D images obtained from FLOT using exposure times of 100 ms, 500 ms, and 2000 ms. (f) Recovered CCD response curve, the solid black line is the fitted curve (x axis is in $\log_e$ scale). (g) Constructed 2D HDR-FLOT image.

Then, demonstration of reconstruction of 3D images were taken. The result is shown in Figure 10. Figure 10(a-c) show the 3D FLOT reconstructed images with exposure times of 100 ms, 500 ms, and 2000 ms. As expected, C3 (lowest concentration) cannot stand out from the background with 100 ms exposure time. Although increasing the exposure time will enhance the SNR of this capillary, the shapes of C2 and C3 get distorted because of overexposure and noise becomes more obvious as shown in Figure 10(c). With 2D HDR fluorescence images, the 3D reconstructed image can resolve all three capillaries with different concentrations of Cy 5.5 simultaneously as shown in Figure 10(d).

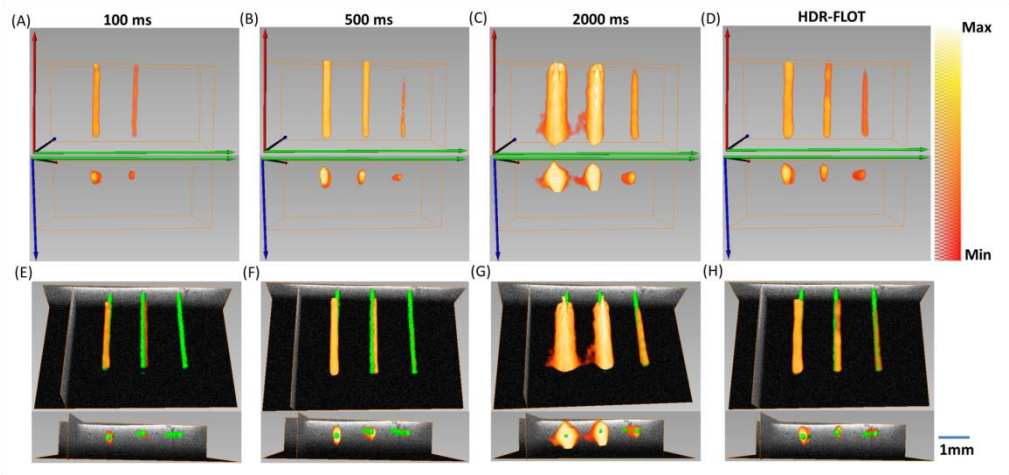

Fig. 10. (a-c) 3D FLOT reconstructed images with exposure time of 100 ms, 500 ms, and 2000 ms. (d) 3D HDR-FLOT reconstructed image. (e-h) Co-registered 3D FLOT reconstructed images with corresponding OCT images (green). The Max in the colormap is the maximum value in the image and Min represents the value: (Background + (Max-Background)/2).

To quantify the relationship between fluorescence intensity and the dye concentration, we performed quantification test by Matlab with custom routine. The normalized average fluorescence intensities of the three capillaries were shown in Figure 11. All the three capillaries from OCT were labelled green for better visualization. The sizes of capillary reconstructed from FLOT were evaluated as the diameter difference ratio (DDR) as: DDR = |D(FLOT) – D(OCT)|/D(OCT). Then the averaged DDR was defined by the mean of three DDRs calculated from the three capillaries, shown in Figure 11. When the exposure time increases, DDR increases, indicating the sizes measured from FLOT deviate from the correct values. HDR-FLOT presents significantly better DDR than any of three exposure time individually.

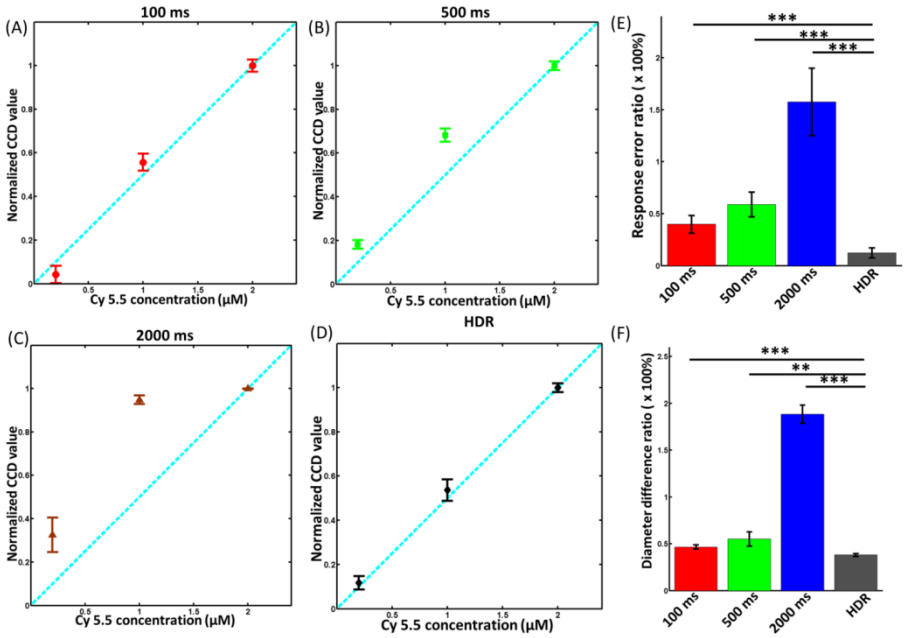

Fig. 11 Average fluorescence intensity of the 3D images as a function of true Cy 5.5 concentration with exposure time 100 ms (A), 500 ms (B), 2000 ms (C), and HDR method (D) . The fluorescence values were normalized to the maximum value (n=50). (E) Average fluorescence response error ratios with different exposure times (n=50). (F) Average diameter difference ratios for FLOT with different exposure time

3.2.3. Conclusion of HDR-FLOT Technique

By demonstrating with fluorescence capillaries inside agar phantom, the performance of HDR-FLOT has proved to have high contrast for a large range of different concentration. This technique has lots of advantages for biomedical applications. First, biological tissue may include different concentration level of fluorescence since targeted tissue may be labeled but other tissues may not, subsurface tissue may be much brighter than deep area. Second, once we reconstructed the camera response curve, we do not have to choose one best exposure time which leads to lots of time of trial. We may just choose several standard exposure times, then apply it to every application. Third, HDR-FLOT can provide high contrast as well as deeper penetration (~20%), which may provide a potential mesoscopic imaging method for imaging neuronal activities in deeper brain.

3.3 Quantification with FLOT

From previous works [19,20], FLOT has been proved to be a bioimaging modality with capability to provide functional information of biomedical targets. However, it is not enough for only visualization with

imaging system for the morphological or structural information of the imaging target, more quantification is needed for further functional study. For FLOT system, it is not the same with some other direct imaging systems, since image reconstruction is taken for 3D image reconstruction which may need to some unpredictable results due to either noises, environment or program parameters for reconstructions. One simple example is that if we reconstruct a stack of noise images without any fluorescence but only flat values, we still can reconstruct an 3D image, which can be regarded as noise image, but it still has a trend of pixel value that the deeper the lower of the value.

To study the availability of quantification with FLOT system and the effects of different depths for intensity changing trends, I took a study with liquid phantom and IR700 dye (IRDye 700DX NHS ester solution). The intralipid concentration was set to provide a reduced scattering coefficient μ_s' = ~0.5 /mm at 635 nm, which is very similar to optical properties of the tumor used in one of our projects, which will be discussed detailed in Chapter 4. Different IR700 concentrations between 0 – 2.5 μM were diluted to test the fluorescence signals at different depths of our FLOT system and the depth profiles do not change much for different IR700 concentration. The result is shown in Figure 12. The raw fluorescence intensity results are shown in Figure 12(a). To subtract the noise and other effects of noise signal generation, I normalized the signal by the signal of non-fluorescence phantom, the normalized signals are shown in Figure 12(b). Since the liquid phantoms are homogenous, the fluorescence signals are supposed to be the same at different depths, while we can notice that there are some decreases in fluorescence as depth increases due to the imperfect reconstruction nature of our FLOT system.

There are some other findings and discussions from this experiment. The first is that the decreasing curve is not exactly for different concentration, that high concentration has fast decreasing rate, but 0.5 μM has little changes. Therefore, we may not provide one line to represent all data with the relationship of changing rate with all concentration, and only proximate value can be achieved if we want to apply this graph to biomedical applications. Second, only depth from 0 – 2 mm provides reasonable information from the reconstructed image. Due to the reconstruction limitation, even there is only little light is received from the

camera, it is hard to separate it from more surface lights during reconstruction. Therefore, the too deep volume in the reconstructed 3D image still include some intensity, but they provide no biological information. And for our applications, we only take the information from 0- 2 mm for count. Third, the background noise is high, which due to the programs of reconstruction we built, further improvements may be taken for this. One quick solution is extracting a weight matrix from the normalized fluorescence intensity of homogenous phantoms at different depths for compensating for the depth-dependent signal decrease from the FLOT system.

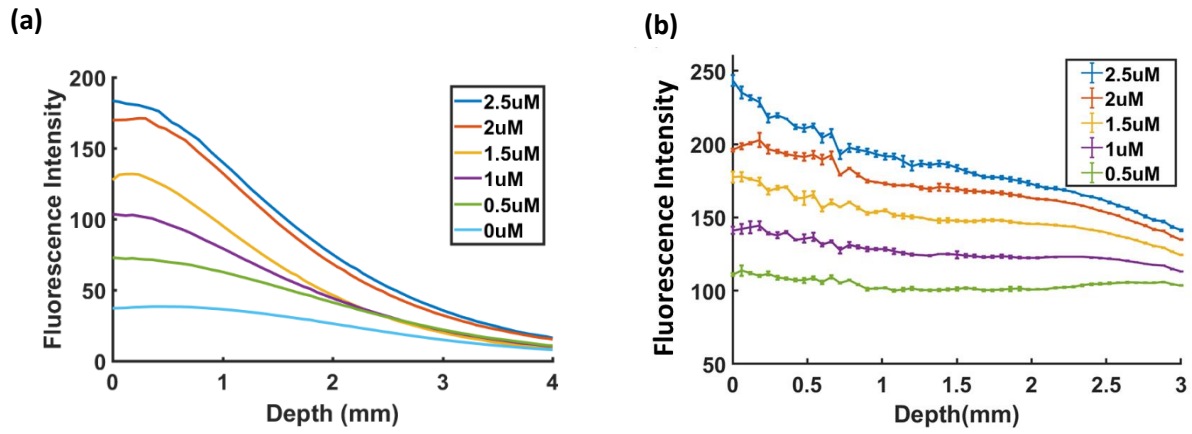

Fig. 12. Relationship between FLOT fluorescence intensity of homogenous phantoms with different IR700 concentrations and imaging depths. (a) Before normalization; (b) after normalization by 0 μM signal.

To demonstrate the quantification capability of FLOT system, I applied it to several datasets of breast cancer tumor fluorescence imaging. One of the fluorescence signal intensity can be seen in Figure 13. We can see that at tumor surface, its fluorescence concentration is close to 1.5 μM since their signal intensities are close, and when the depth going deep, its intensity is decreasing faster than the phantoms, which due to the decrease of fluorescence concentration, when the depth is deeper than 1.8 mm, its concentration is below 0.5 μM. From this experiment, we have demonstrated that FLOT has availability for quantification of fluorescence concentration in biomedical application. Even though, we have not yet figured out a way to build a model to accurately calculate its concentration, it is possible to take more quantitative work and experiments to build a mathematical model in the future.

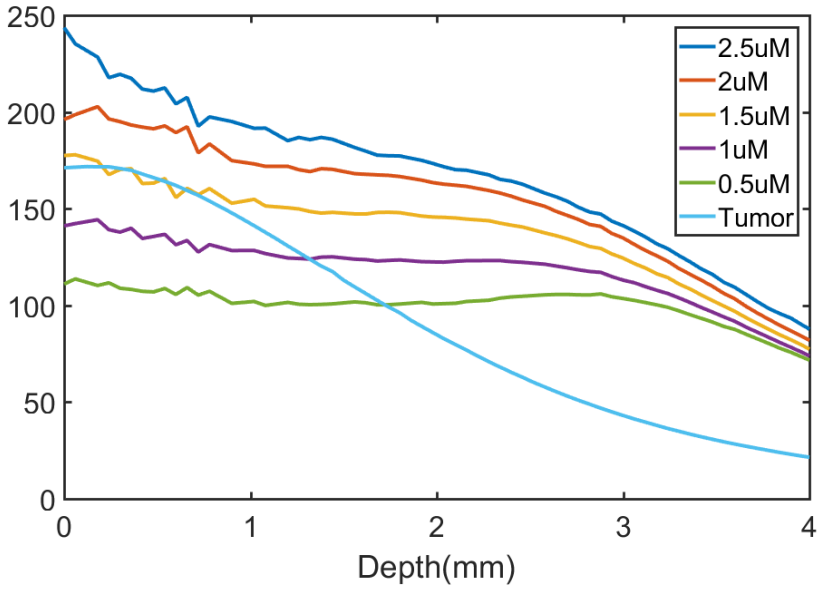

Fig. 13. Fluorescence intensity of cancer tumor and homogenous phantoms.

Another parameter to be considered is the scattering coefficient of the sample. To demonstrate the effects of the scattering coefficient to the reconstructed image results. I made three scattering phantoms with 2%, 1% and 0.5% of intralipid as well as 2 μM IR700. For the reconstruction, all parameters set for the algorithm are the same. The depth profile of reconstructed images is shown in Figure 14. We can see that the scattering coefficient may affect the reconstruction results that larger scattering may have higher signal at surface area but on the contrary, have lower signal in the deep area. This effect is not difficult to explain, that higher scattering will lead to more light reflected when light propagates through the sample, and its power will decay faster when it goes deep. Therefore, at sub-surface area, we can see higher intensity, and at deep area, it is opposite. Since the scattering coefficient may affect the intensity of the reconstructed images, to quantify biomedical samples, we need to use the same scattering coefficient material for phantom fabrication.

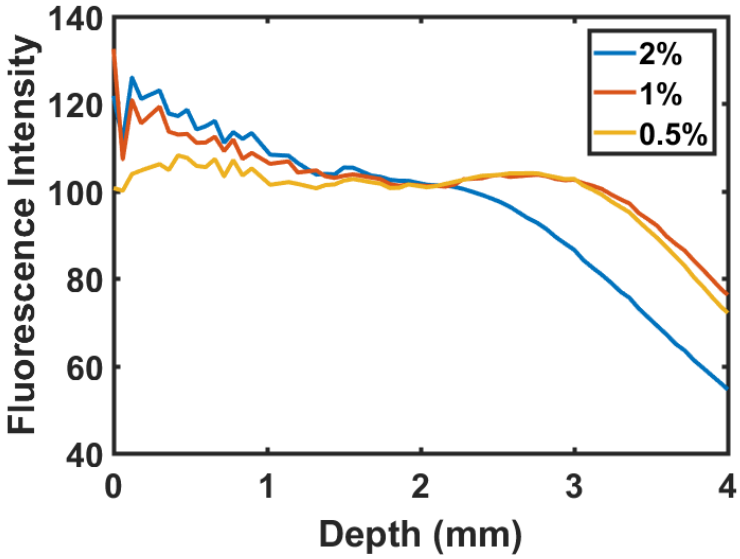

Fig. 14. Depth profile of three fluorescence phantoms with different scattering coefficient. The scattering media intralipid is set to be 2%, 1% and 0.5%.

Chapter 4: Biomedical Applications of Fluorescence Laminar Optical Tomography

This chapter will discuss several biomedical applications of aFLOT, including tissue engineering, neural science and cancer detection.

4.1 Tissue Engineering

Regenerative medicine has emerged as an important discipline which aims at introducing living cells or functioning tissues to repair injury or replace damaged tissues or organs which lose functions. Optimization of regenerative medicine strategies includes the design of biomaterials, cell-seeding methods, cell-biomaterial interactions, and molecular signaling within the engineered tissue. The current gold standard method for quantifying the 3D-cell distribution during tissue engineering is fluorescence confocal microscopy. It can visualize cells and molecules via a wide variety of fluorescence probes. However, the limitation is its penetration depth, which is only ~ 100 μm [26]. One approach to solve this problem may include 3D image recompiling and cryo-sectional scaffolds [27]. Although robust, this approach is destructive and time-consuming, FLOT with ~2 mm imaging depth may solve this problem and applied to tissue engineering scaffolds imaging [28 - 30].

Human mesenchymal stem cells (hMSCs) is applied as cell model for this project, they were cultured in control media consisting of Dulbecco's Modified Eagle Medium supplemented with 10% fetal bovine serum. CellTacker Orange CMRA Dye 548/576 nm is utilized to label the cells inside tissue engineered scaffolds. The cells concentration is set to be 0.015, 0.05, 0.1, 0.5, 1 and 2 million cells/ml. From the imaging results, we may clearly see the differences of cell concentration, with a custom defined threshold. And the normalized cell numbers are consistent with the real cell numbers in the scaffold. From this research, FLOT has been demonstrated of capable of imaging and quantifying cell numbers and concentration in tissue engineering. Our group has also taken some further research into this topic for quantifying the

distribution and migration during tissue engineering process [29]. Some future research may include in vivo fluorescence imaging and long-term monitoring.

4.2 Neural Activity

Another interesting topic of FLOT applications is neural functional imaging of brain activity. Voltage-sensitive dye imaging (VSDi) has been quite useful in imaging activities of the neural networks in the brain [31]. VSDi is based on fluorophore molecules that bind to the neural membrane and convert changes in transmembrane voltage into the fluorescence of the emitted light [32]. In this research, FLOT is combine with VSDi for brain functional imaging, neural activity is evoked in the whisker barrel cortex of mice by deflection of a single whisker in vivo with 5 ms temporal resolution. Then, FLOT recording is taken after each stimulation, and a 3D reconstruction is performed after that. From this research, FLOT has demonstrated its capability for neural functional imaging with its high recording speed and relatively deep penetration depth.

4.3. Cancer Detection

The efficacy of cancer therapy depends on its ability to deliver drugs to tumors [33]. Targeted cancer therapies offer the promise of more effective tumor control with fewer side effects than conventional cancer therapies. Molecular therapies based on monoclonal antibodies (mAbs) are highly selective for tumors expressing specific antigens. Combinations of conventional photosensitizers and mAbs have been tested, but the improvement in selectivity is still limited [34-37]. Photoimmunotherapy (PIT) is an emerging low side effect cancer therapy based on a targeted monoclonal antibody-photo absorber conjugate (APC) that induces rapid cellular necrosis after exposure to NIR light. IR700 is not only fluorescent, and thus can be used as an imaging agent, but it also is phototoxic serving as an imaging theragnostic. When exposed to intense levels of NIR light, the conjugate becomes lethal, but only to those cells to which it is bound [38].

NIR light exposure can lead to rapid, target-selective necrotic cell death in vitro and effective tumor shrinkage on animal models in vivo. PIT induced highly selective cancer cell death, while leaving most of the rumor blood vessels unharmed, leading to an effect termed super enhanced permeability and retention, which significantly improved the effectiveness of anticancer drugs [39].

Previously, we have investigated the micro distribution of APCs at different locations and depths during and after PIT effects in vivo by using a custom 2D fluorescence imaging system and two-photon microscopy [40], since it will be more interesting if we can acquire 3D imaging of PIT process to understand deeper into the mechanism, we applied our FLOT system for APCs imaging during and after PIT process [41]. Optical coherence Tomography (OCT) is an established biomedical imaging method for subsurface imaging od tissues microstructure with high resolution (<10μm) and 1-2 mm penetration depth [42]. We introduced OCT to this project to provide a 3-D morphological imaging of the target tumor as FLOT for functional imaging.

Figure 14 Showed the results of 3D tumor volume during and after PIT process. OCT with high resolution can provide clear morphological structure of the tumor volume as well as surrounding tissue. Reconstructed 3D FLOT image is registered to OCT images for better understanding of the locations of fluorescence shown in the image. From the Figure 15(e) we can see the fluorescence intensity difference of tumor surface and deeper tumor. This work is based on the work shown in Chapter 3 of quantification with FLOT. Even though an accurate curve of the relationship of reconstructed fluorescence intensity with depth is hard to build, it is available for us to quantify only two areas, the surface and deep area, instead of every depth.

Figure 15(f) showed the intensity changing during and after PIT. At 0 minute, NIR LED irradiation began and the IR700 fluorescence intensity dropped quickly at both tumor surface and deep area in the first 20 minutes. Then, the LED is turned off and PIT treatment was done. The fluorescence intensity began to recover and increased over the initial value which means that the drug accessed more tumor areas after PIT treatment.

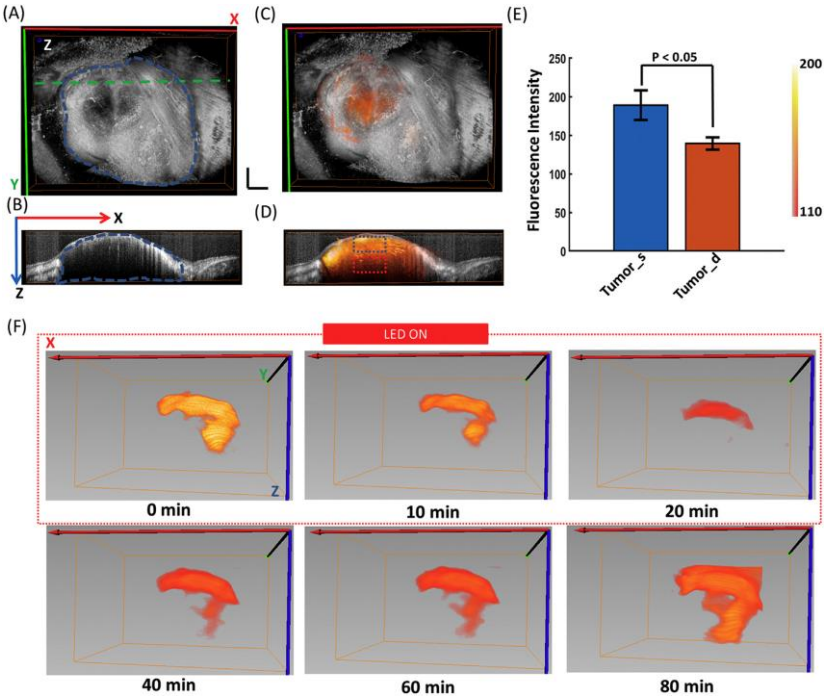

Fig. 15. (a-d) Top-view and side-view of tumor volume; (e) IR700 fluorescence intensity value of tumor surface and deep area; (f) IR700 fluorescence intensity during and after PIT.

Being able to quantitatively monitor 3D image of fluorescent distribution and therapeutic effects in vivo in real time helps us further understanding the PIT mechanism as well as drug delivery system. FLOT has been demonstrated to be a promising 3D fluorescence imaging technique for more biomedical applications with its capability for deep tissue imaging.

Figure 16 showed the depth profile of fluorescence intensity of tumor during and after PIT treatment. From this figure, we can see that both surface and deep area has fluorescence intensity decreasing during 0 to 20 minutes. And only surface has continuing decrease during 20 to 40 minutes. Then, the recovery showed at around 80 minutes. This dataset is consistent to the 3D images shown in Figure 15, we may see the difference of fluorescence changing trend for surface and deep area. One reason for longer PIT effect is due to the closer to the surface the more power of light is absorbed by the tumor, so the fluorescence is decreasing more and longer because more tumor cells are killed at this area. Both surface and deep area has

some recovery, but the intensity is still lower than initial time, which is because of the photo bleaching effect.

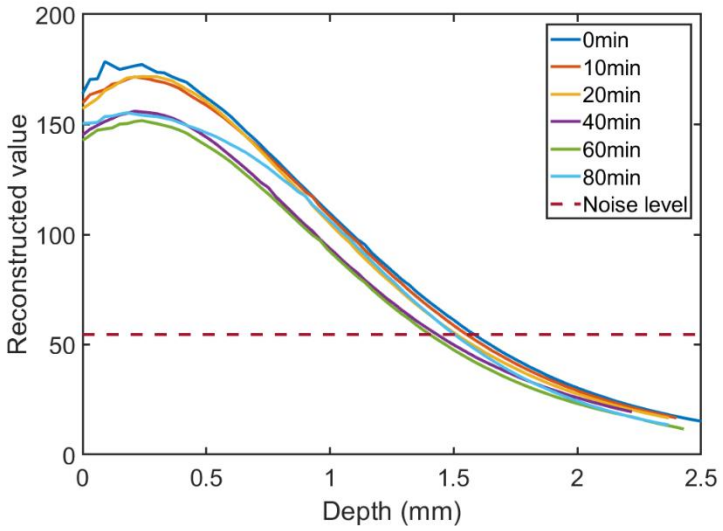

Fig. 16. Depth profile of fluorescence intensity of cancer tumor during and after PIT treatment.

We have also tested the photobleach effects on the signal changing without PIT treatment. The same mouse and cancer model are taken for this test. The depth profile of this control group data is shown in Figure 17. I normalized the noise value to 1, then we achieved this figure by the signal-to-noise ratio. From this graph, we can see that during 0 to 40 minutes, there is no significant changes of the signal values. By taking three mice as control group, we found similar results. Therefore, we can conclude that the photobleach effects for IR700 with this cancer tumor model has no significant photobleach effects.

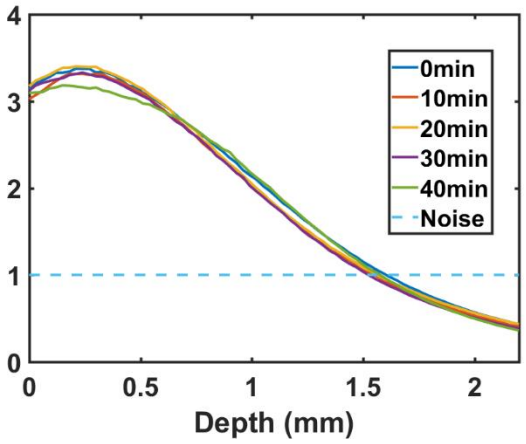

Fig. 17. Depth profile of fluorescence intensity of control group. The intensity is normalized by the noise level, the y-axis is signal-to-noise ratio.

Chapter 5: Conclusion and Future Work

Since FLOT is a novel bioimaging modality with capability of high-speed 3D imaging of up to 2 mm imaging depth, it has a promising potential for bioscience research as well as clinical applications. For better assessment of performance of FLOT and other imaging systems, better methods for phantom fabrications need to be researched to mimic more realistic biomedical models. Some improvements may also be taken to get better resolution or imaging depth of FLOT to achieve better images. This thesis has demonstrated wide applications of FLOT technique, and the potential of bioimaging for biology and medical research.

Future work based on this thesis could including the following several topics:

First, we may research into the possibility design and fabrication of biomimetic phantoms for other biomedical models with 3D print technique. Since 3D print technique has a huge advantage of fabrication of any complex design with low time and money cost. It can be applied to more and more biomedical research field, either as mechanical components or as phantoms for biomedical devices testing.

Second, we may improve our HDR algorithm, integrate the algorithm to the FLOT setup we have now to make it applicable for all different samples with FLOT imaging recording. Since photo bleaching is a factor which may affect the results of fluorescence imaging in some situation. It is necessary to record FLOT images in shorter time, once we improved the algorithm, it may take ~50% time for image recording.

Third, there are deviation between the imaging targets and reconstructed images, due to some simplification of mathematical models of reconstruction. It may be worthy if we can figure out ways to improve our reconstruction methods to improve the results. One problem is the cross talk between each point in the line beam for illumination. I found that the resolution in the direction of parallel to illumination is worse than perpendicular direction, seen in Figure 18. In Figure 18(b), the 0 degree and 180 degree illumination on quantum dots is taken, we can see these two different angles will lead to different resolution in different directions. The reason for this difference could be either the illumination angle or the line beam

illumination cross talk. Some solutions may be imaging with different angles and directions and overlapping all the data to acquire better image qualities in all direction. This may be an interesting topic for FLOT technique improvement.

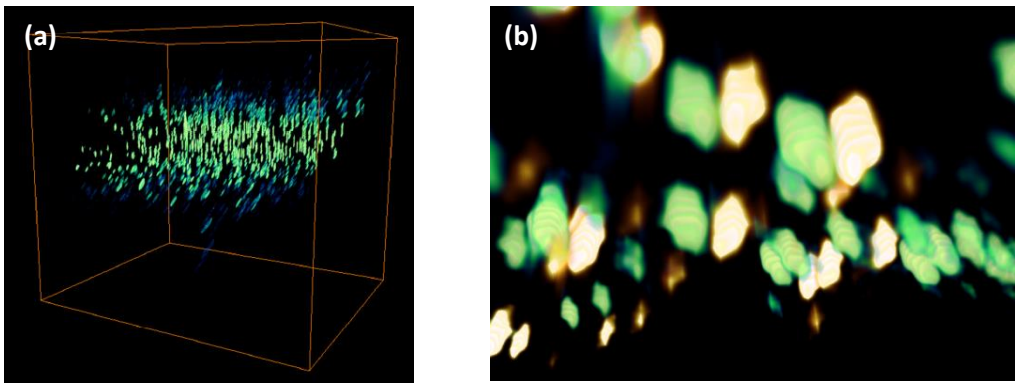

Fig. 18. (a) The difference of resolution in different direction. (b) Two reconstructed images on the same quantum dots phantom

Last, 2 mm penetration depth is not enough for every biomedical application, for some *in vivo* imaging applications, we may need to design an endoscopic FLOT system. It can be integrated with laparoscope or other medical endoscopic system. However, it is not easy for scanning using a fiber or fiber bundle, we changed the illumination from 45 degree to 90 degree to the sample to achieve higher efficiency for the fiber bundle. A 4 mm * 4 mm fiber bundle shown in Figure 19(a) is applied for this project. The system setup is shown in Figure 19(b). The major challenge here is still the light propagation in the fiber, since the reflected fluorescence lights are random angled, only a small proportional signal of them can propagate through the fiber bundle to the camera. More research needs to be taken to solve this problem.

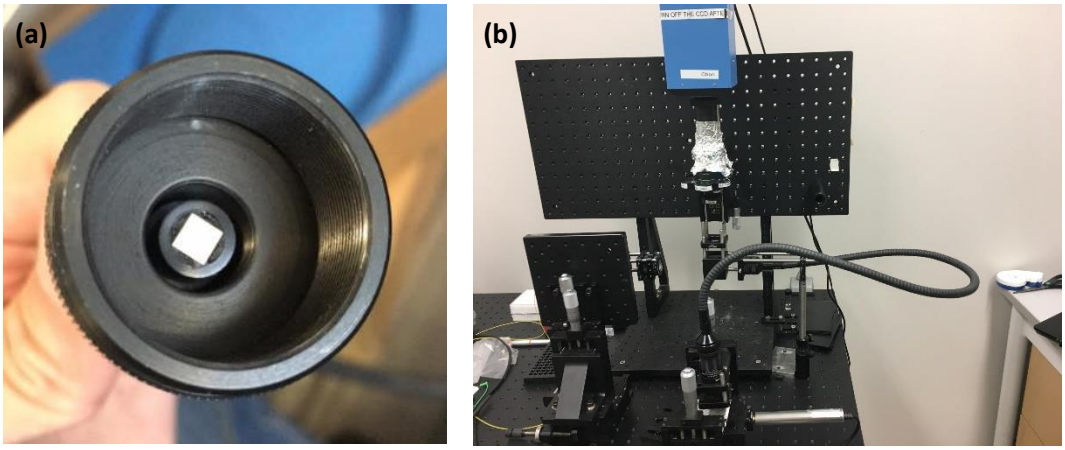

Fig. 19. (a) 4 mm * 4 mm fiber bundle; (b) endoscopic FLOT system with the fiber bundle shown in Figure 19(a).

Bibliography

1. *Light Microscopy*. Nature Milestones. MacMillan Publishers Limited, 6-22 (2009).
2. Liu, Y., Ghassemi, P., Depkon, A., Iacono, M.I., Lin, J., Mendoza, G., Wang, J., Tang, Q., Chen, Y. and Pfefer, T.J., *Biomimetic 3D-printed neurovascular phantoms for near-infrared fluorescence imaging*. Biomedical Optics Express, 9(6), pp.2810-2824 (2018).
3. Pfefer, T. J. and Agrawal, A., *A review of consensus test methods for established medical imaging modalities and their implications for optical coherence tomography*, Proc. SPIE 8215, 82150D (2012).
4. Gavrielides, M. A., Zeng, R., Kinnard, L. M., Myers, K. J., and Petrick, N., *Information-theoretic approach for analyzing bias and variance in lung nodule size estimation with CT: a phantom study*, IEEE Trans. Med. Imaging 29(10), 1795–1807 (2010).
5. Iacono, M. I., Neufeld, E., Akinnagbe, E., Bower, K., Wolf, J., Vogiatzis Oikonomidis, I., Sharma, D., Lloyd, B., Wilm, B. J., Wyss, M., Pruessmann, K. P., Jakab, A., Makris, N., Cohen, E. D., Kuster, N., Kainz, W. and Angelone, L. M., *MIDA: a multimodal imaging-based detailed anatomical model of the human head and neck*, PLoS One 10(4), e0124126 (2015).
6. Bücking, T. M., Hill, E. R. Robertson, J. L., Maneas, E., Plumb, A. A. and Nikitichev, D. I., *From medical imaging data to 3D printed anatomical models*, PLoS One 12(5), e0178540 (2017).
7. Prahl, S. A., van Gemert, M. J. C. and Welch, A. J., *Determining the optical properties of turbid mediaby using the adding-doubling method*, Appl. Opt. 32(4), 559–568 (1993).
8. Cheong, W., *Summary of Optical Properties*, in Optical-Thermal Response of Laser-Irradiated Tissue, (Plenum Press:1995).
9. van der Zee, P., Essenpreis, M. and Delpy, D. T., *Optical properties of brain tissue*, Proc. SPIE 1888, 454–465 (1993).
10. Marshall, M. V., Rasmussen, J. C., Tan, I. C., Aldrich, M. B., Adams, K. E., Wang, X., Fife, C. E., Maus, E. A., Smith, L. A. and Sevick-Muraca E. M., *Near-infrared fluorescence imaging in humans with indocyanine green: a review and update*, Open Surg. Oncol. J. 2(2), 12–25 (2010).
11. Killory, B. D., Nakaji, P., Gonzales, L. F., Ponce, F. A., Wait, S. D. and Spetzler, R. F., *Prospective evaluation of surgical microscope-integrated intraoperative near-infrared indocyanine green angiography during cerebral arteriovenous malformation surgery*, Neurosurgery 65(3), 456–462 (2009).
12. Liebert, A., Wabnitz, H., Obrig, H., Erdmann, R., Möller, M., Macdonald, R., Rinneberg, H., Villringer, A. and Steinbrink, J., *Non-invasive detection of fluorescence from exogenous chromophores in the adult human brain*, Neuroimage 31(2), 600–608 (2006).
13. Kacprzak, M., Liebert, A., Sawosz, P., Żołek, N., Milej, D. and Maniewski, R., *Time-resolved imaging of fluorescent inclusions in optically turbid medium—phantom study*, Opto-Electron. Rev. 18(1), 37 (2010).
14. Milej, D., Gerega, A., Zołek, N., Weigl, W., Kacprzak, M., Sawosz, P., Mączewska, J., Fronczewska, K., Mayzner-Zawadzka, E., Królicki, L., Maniewski, R. and Liebert, A., *Time-resolved detection of fluorescent light during inflow of ICG to the brain-a methodological study*, Phys. Med. Biol. 57(20), 6725–6742 (2012).
15. Zaidi, H. A., Abla, A. A., Nakaji, P., Chowdhry, S. A., Albuquerque, F. C. and Spetzler, R. F., *Indocyanine green angiography in the surgical management of cerebral arteriovenous malformations: lessons learned in 130 consecutive cases*, Neurosurgery 10(2), 246–251 (2014).
16. Korhonen, V. O., Myllyla, T. S., Kirillin, M. Y., Popov, A. P., Bykov, A. V., Gorshkov, A. V., Sergeeva, E. A., Kinnunen, M. and Kiviniemi, V., *Light propagation in NIR spectroscopy of the human brain*, IEEE J. Sel. Top. Quantum Electron. 20(2), 289–298 (2014).

17. Tang, Q., Liu, Y., Tsytsarev, V., Lin, J., Wang, B., Kanniyappan, U., Li, Z. and Chen, Y., *High-dynamic-range fluorescence laminar optical tomography (HDR-FLOT)*. Biomedical optics express, 8(4), pp.2124-2137 (2017).
18. Hillman, E.M., Boas, D.A., Dale, A.M. and Dunn, A.K., *Laminar optical tomography: demonstration of millimeter-scale depth-resolved imaging in turbid media*. Optics letters, 29(14), pp.1650-1652 (2004).
19. Chen, C.W. and Y. Chen, *Optimization of Design Parameters for Fluorescence Laminar Optical Tomography*. Journal of Innovative Optical Health Sciences, 4(3): p. 309-323 (2011).
20. Chen, C.W., et al. *Three-dimensional imaging of stem cell distribution within tissue engineering scaffolds using angled fluorescent laminar optical tomography (aFLOT)*. Photonics Conference (PHO), (2011).
21. Robertson, M. A., Borman, S. and Stevenson, R. L., *Estimation-theoretic approach to dynamic range enhancement using multiple exposures*, J. Electron. Imaging 12(2), 219–228 (2003).
22. Madden, B. C., *Extended intensity range imaging*, Technical Report, GRASP Laboratory, University of Pennsylvania (1993).
23. Debevec P. E. and Malik, J., *Recovering high dynamic range radiance maps from photographs*, in ACM SIGGRAPH 2008 classes (ACM), p. 31 (2008).
24. Lian, L., Deng, Y., Xie, W., Xu, G., Yang, X., Zhang, Z. and Luo, Q., *High-dynamic-range fluorescence molecular tomography for imaging of fluorescent targets with large concentration differences*, Opt. Express 24(17), 19920–19933 (2016).
25. Fei, P., Yu, Z., Wang, X., Lu, P. J., Fu, Y., He, Z., Xiong, J. and Huang, Y., *High dynamic range optical projection tomography (HDR-OPT)*, Opt. Express 20(8), 8824–8836 (2012).
26. Tan, W., Sendemir-Urkmez, A., Fahrner, L. J., Jamison, R., Leckband, D., and Boppart, S. A. *Structural and functional optical imaging of three-dimensional engineered tissue development*. Tissue Engineering,10(11-12), 1747–1756 (2004).
27. Thevenot, P., Nair, A., Dey, J., Yang, J., and Tang, L. P., *Method to analyze three-Dimensional cell distribution and infiltration in degradable scaffold*s. Tissue Engineering Part C-Methods, 14(4), 319–331 (2008).
28. Zhao, L. L., Lee, V. K., Yoo, S. S., Dai, G. H., and Intes, X., *The integration of 3- D cell printing and mesoscopic fluorescence molecular tomography of vascular constructs within thick hydrogel scaffolds*. Biomaterials, 33(21), 5325–5332 (2012).
29. Ozturk, M. S., Lee, V. K., Zhao, L. L., Dai, G. H., and Intes, X., *Mesoscopic fluorescence molecular tomography of reporter genes in bioprinted thick tissue*. Journal Of Biomedical Optics, 18(10), 100501 (2013).
30. Tang, Q., Piard, C., Lin, J., Nan, K., Guo, T., Caccamese, J., Fisher, J. and Chen, Y., *Imaging stem cell distribution, growth, migration, and differentiation in 3 -D scaffolds for bone tissue engineering using mesoscopic fluorescence tomography*. Biotechnology and bioengineering, 115(1), pp.257-265 (2018).
31. Bjorn, S., Englmeier, K. H., Ntziachristos, V. and Schulz, R. *Reconstruction of fluorescence distribution hidden in biological tissue using mesoscopic epifluorescence tomography*. J Biomed Opt 16, 046005; doi: 10.1117/1.3560631 (2011).
32. Tsytsarev, V., Bernardelli, C. and Maslov, K. I. *Living Brain Optical Imaging: Technology, Methods and Applications*. J Neurosci Neuroeng 1, 180–192 (2012).
33. Nagaya, T., Nakamura, Y., Sato, K., Harada, T., Choyke, P. L., Kobayashi, H., *Improved micro-distribution of antibody-photon absorber conjugates after initial near infrared photoimmunotherapy (NIR-PIT)*, J. Control. Release 232-1-8(2016).
34. Mew, D., Wat, C.K., Towers, G.H., Levy, J.G., *Photoimmunotherapy: treatment of animal tumors with tumor-specific monoclonal antibody-hematoporphyrin conjugates*, J. Immunol. 130 1473–1477 (1983).
35. Rosenkranz, A.A., Jans, D.A., Sobolev, A.S., *Targeted intracellular delivery of photosensitizers to enhance photodynamic efficiency*, Immunol. Cell Biol. 78 452–464 (2000).

36. Carcenac, M., Dorvillius, M., Garambois, V., Glaussel, F., Larroque, C., Langlois, R., Hynes, N.E., van Lier, J.E., Pelegrin, A., *Internalisation enhances photo-induced cytotoxicity of monoclonal antibody- phthalocyanine conjugates*, Br. J. Cancer 85 1787–1793 (2001).
37. Vrouenraets, M.B., Visser, G.W.M., Stewart, F.A., Stigter, M., Oppelaar, H., Postmus, P.E., Snow, G.B., van Dongen, G.A.M.S., *Development of meta-tetrahydroxyphenylchlorin-monoclonal antibody conjugates for photoimmunotherapy*, Cancer Res. 59 1505–1513 (1999).
38. Mitsunaga, M., Ogawa, M., Kosaka, N., Rosenblum, L.T., Choyke, P.L., Kobayashi, H., *Cancer cell-selective in vivo near infrared photoimmunotherapy targeting specific membrane molecules*, Nat. Med. 17 1685–1691 (2011).
39. Sano, K., Nakajima, T., Choyke, P.L., Kobayashi, H., *Markedly enhanced permeability and retention effects induced by photo-immunotherapy of tumors*, ACS Nano 7 717–724 (2013).
40. Tang, Q., Nagaya, T., Liu, Y., Lin, J., Sato, K., Kobayashi, H. and Chen, Y., *Real-time monitoring of microdistribution of antibody-photon absorber conjugates during photoimmunotherapy in vivo*. Journal of Controlled Release, 260, pp.154-163 (2017).
41. Tang, Q., Nagaya, T., Liu, Y., Horng, H., Lin, J., Sato, K., Kobayashi, H. and Chen, Y., *3D mesoscopic fluorescence tomography for imaging micro-distribution of antibody-photon absorber conjugates during near infrared photoimmunotherapy in vivo*. Journal of controlled release, 279, pp.171-180 (2018).
42. Tang, Q., Wang, J., Frank, A., Lin, J., Li, Z., Chen, C.-w., Jin, L., Wu, T., Greenwald, B.D., Mashimo, H., Chen, Y., *Depth-resolved imaging of colon tumor using optical coherence tomography and fluorescence laminar optical tomography*, Biomed. Opt. Expr. 7 5218–5232 (2016).